High flux source of cold rubidium atoms

Christopher Slowe[a)]
Department of Physics and Division of Engineering and Applied Sciences, Harvard University, Cambridge, Massachusetts 02138

Laurent Vernac
Department of Physics and Division of Engineering and Applied Sciences, Harvard University, Cambridge, Massachusetts 02138 and Laboratoire de Physique des Laser, Institut Galilée, Université Paris 13, Avenue Jean Baptiste Clément 93430, Villetaneuse, France

Lene Vestergaard Hau
Department of Physics and Division of Engineering and Applied Sciences, Harvard University, Cambridge, Massachusetts 02138

We report on the production of a continuous, slow, and cold beam of ^{87}Rb atoms with an extremely high flux of 3.2×10^{12} atoms/s, a transverse temperature of 3 mK, and a longitudinal temperature of 90 mK. We describe the apparatus created to generate the atom beam. Hot atoms are emitted from a rubidium candlestick atomic beam source and transversely cooled and collimated by a 20 cm long atomic collimator section, boosting overall beam flux by a factor of 50. The Rb atomic beam is then decelerated and longitudinally cooled by a 1 m long Zeeman slower. © *2005 American Institute of Physics.* [DOI: 10.1063/1.2069651]

I. INTRODUCTION

Cold and slow, high-flux atomic beams are essential for high signal-to-noise measurements in atom interferometry experiments,[1] for efficient loading of magneto-optical traps (MOTs) for rapid production of Bose-Einstein condensates with large atom numbers, and for the creation of a cw atom laser. A variety of methods has been employed in recent years to create cold, intense atomic beams. Low-velocity intense sources,[2] Axicons,[3] and two-dimensional (2D) MOTs[4–6] are typically limited in total flux to a few times 10^9 atoms/s.

White-light slowing has been used to produce a beam with a flux of up to 2×10^{10} Cs atoms/s.[7] With use of a Zeeman slower,[8,9] tunable-velocity beams with high intrinsic brightness have been generated,[10] while the authors in Ref. 11 have very recently been able to produce a beam of Rb with an integrated total flux of 2×10^{11} atoms/s, with the aim to produce a cw atom laser by continuous evaporation. In pursuit of this goal, in this article, we report on a further dramatic increase in overall flux with the production of a slow and cold (both transversely and longitudinally) atomic beam with a total flux of $3.2 \times 10^{12}(1.7 \times 10^{12})$ atoms/s at 116(45) m/s and a peak intensity of $7.5 \times 10^{11}(3 \times 10^{11})$ atoms/s/cm^2, thus increasing the flux by more than an order of magnitude. We describe in detail the apparatus created for achieving such high flux values.

II. EXPERIMENTAL APPARATUS

A schematic representation of the setup used for production of the atomic beam is shown in Fig. 1. It consists of a two-stage vacuum chamber, with the source chamber separated from the detection chamber by a 1 m Zeeman-slower tube.

In the source chamber, an atomic beam of Rb is produced by means of a candlestick atomic beam source[12,13] (described in detail in Sec. II A). Because of the low operating temperature required with the candlestick source, except for the localized emission point, we are able to keep our source chamber pressure at or below 10^{-8} Torr under operating conditions. Much of the excess rubidium is cryopumped away with the aid of a "cold finger," which is kept at $-45\ ^\circ$C and which wraps around the back of the oven (not shown in the figure).

At the output of the source and in the same chamber, we have implemented 20 cm of transverse cooling via a 15 cm atomic collimator[14,15] and 5 cm of 2D optical molasses. As we will describe in detail in Sec. II B, the collimator is based on recycling the power from a 1 cm wide laser beam by means of a cavity with up to 50 reflections, which is possible only because we are able to maintain such a low vapor pressure in this section of the chamber, keeping background absorption and laser attenuation to a minimum.

In the final stage of production, the atomic beam is longitudinally slowed and cooled by means of a Zeeman slower (Sec. II C), which allows us to tune the final atomic beam velocity continuously from 45 to 120 m/s.

Detection is performed in a region 10 cm beyond the end of the Zeeman slower via an optical density measurement of the resulting atomic beam. By varying the angle of the probe laser beam used in this measurement, we are able to extract the full velocity and spatial distribution of the atomic beam.
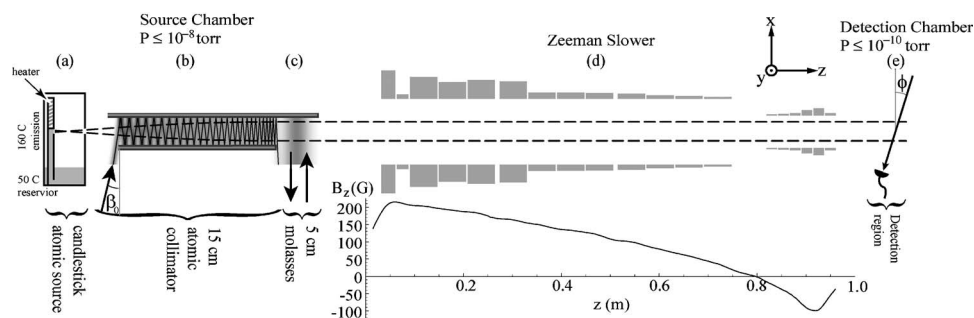
---

a)Electronic mail: slowe@physics.harvard.edu

FIG. 1. Experimental setup. An atomic beam is produced via a candlestick atomic beam source (a) with a divergence angle of 1/10 radian. The atoms in the beam then pass through a 20 cm long transverse collimation (b) and cooling (c) stage and are subsequently longitudinally decelerated and cooled by means of a 1 m long Zeeman slower (d), which is designed in the zero-crossing configuration shown. Measurement of the atomic beam is performed via an absorption measurement 10 cm beyond the end of the Zeeman slower (e).

A. The candlestick atomic beam source

Our source of thermal atoms originates from a Rb candlestick atomic-beam source [Figs. 1(a) and 2],[12,13] which provides an intense, well collimated beam. This source has a low-temperature shield surrounding a localized hot emission point. The 2 mm emission hole lies 2 cm behind a 2 mm collimation hole, resulting in an emitted beam with a total divergence of $\pi/50$ sr. Rb at the emission hole is replenished by capillary action via a stainless steel mesh wick,[16] which draws from a reservoir of liquid rubidium. Since the reservoir need only be kept at the melting point of Rb, the pressure of the surrounding chamber can be kept below 10^{-8} Torr.
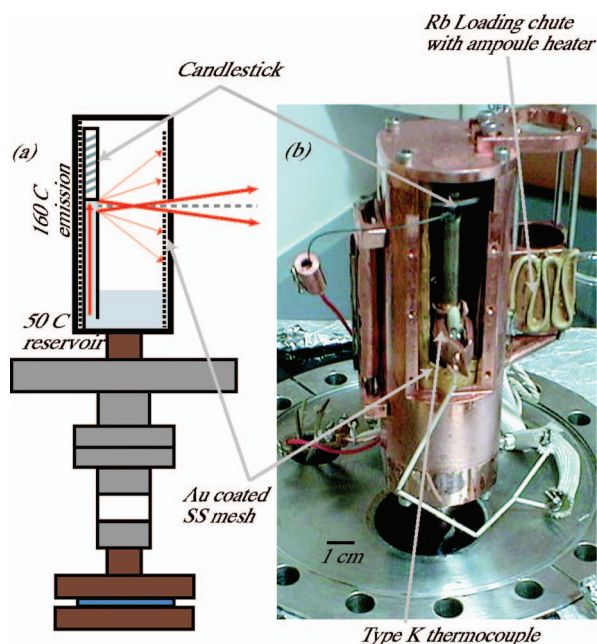

FIG. 2. Candlestick atomic beam source. (a) Schematic. Rubidium is wicked up a 5 mm wick made of gold-coated stainless steel from a molten reservoir, evaporated, and effused through a 2 mm emission point. Rb emitted outside of a 1/10th radian half-angle cone is recycled by more gold-coated mesh that lines the inside of the canister. (b) The actual device shown from the back (atomic beam would point into the article). To monitor the temperature, a Type K thermocouple encased in an alumina housing is attached to the back of the molybdenum candlestick. Rb is loaded into the canister by means of the loading chute, shown at right, which is designed for 5 g ampoules.

To produce a wick that liquid Rb will readily wet, we plate the mesh directly with a uniform 0.2 μm layer of gold with no intermediate adhesion layer. We use a 20 mA/cm^2 current density during 5 min of electroplating using Orosene 999 Gold solution.[17] The rubidium wets and subsequently dissolves this thin gold layer, and is then able to wet the clean stainless steel surface underneath.

The wick itself consists of a 5 mm diameter roll of approximately 15 layers of mesh, which is inserted into a molybdenum candlestick (as shown in Fig. 2). Molybdenum is chosen for its low outgassing rate at the high temperatures used. Moreover, by lining the inside of the Rb-reservoir canister with a double layer of the same mesh material, any Rb that does not make it through the collimation hole can be recycled, decreasing the need for reloading and source maintenance due to clogging.

The emission point is heated with a 0.25 mm tungsten-rhenium wire filament,[18] which is wrapped onto an alumina shaft and inserted into the top of the molybdenum candlestick (identical to the design in Ref. 12). The canister itself is separately temperature regulated by mounting it on a 0.75 in. solid-copper vacuum feed-through connected to a water-cooled thermoelectric cooler (TEC). The cooler can be run in either heating or cooling mode, and using the combination of heater and TEC, we may set the temperature of the emission point and the reservoir completely independently.

To load the source, we have built into the side of the candlestick's canister a loading chute as well as a holder for a 5 g Rb ampoule, which has its own heater. We break this prescored glass ampoule in an argon-filled plastic bag and then transfer it into the source chamber (from a top flange), which also has been filled with argon. To load Rb from the ampoule into the main reservoir, the ampoule is heated until its contents melt and pour into the canister, which is simultaneously heated to 50 °C (the melting point of Rb is 40 °C). To start the wetting process, we bring the canister temperature up to 60 °C and the emission hot spot to 80 °C for 24 h until the mesh can be seen to be uniformly coated with rubidium. Typically, emission requires a "kick start" whereby the reservoir is maintained at or below 55 °C and the emission point is brought up to 180 °C. At this temperature, emission can be verified by the use of a crystal thickness monitor situated 25 cm from the collimation hole.
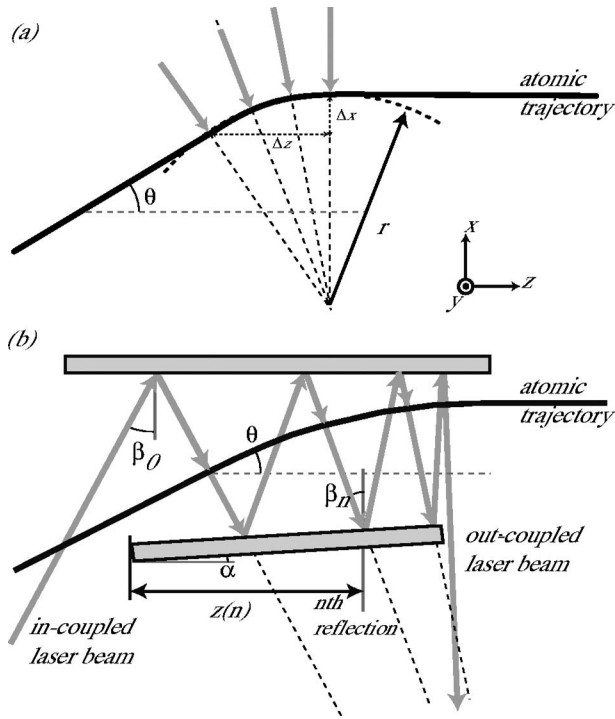
FIG. 3. Schematic of transverse atom collimation. (a) Ideal setup, in which the atoms are uniformly accelerated normal to their velocity and deflected on a circular arc. In this idealized scenario, the collimating laser beams would be uniformly spaced and would have their angle vary linearly with position (z). (b) Actual setup, in which case the density of the laser rays will increase down the collimator. In this way, the angle of the collimating laser beam with respect to the mirror normal will vary nonlinearly with z as in Eq. (6), and the optical wavefronts will deviate from a circle.

At the emission point operating temperature of 160 °C, the resulting atomic beam has a mean velocity of 400 m/s, and a total flux of 1.2×10^{14} atoms/s; 25% of these emitted atoms are ^{87}Rb, of which 36% are within the designed capture velocity range of the Zeeman slower (320 m/s), for a total available flux of 1.1×10^{13} atoms/s.

B. Transverse cooling

Although the atomic beam produced by the candlestick has a small divergence angle, the solid angle subtended by the Zeeman slower as viewed from the candlestick is yet another two orders of magnitude smaller. Moreover, the tenth of a radian divergence angle of the atomic beam translates into a transverse velocity spread of the atoms of several tens of meters per second rms, which becomes comparable with the longitudinal velocity as the beam is decelerated, and would lead to dramatic atomic beam spreading at the end of the Zeeman slower. To compensate for this, we efficiently couple the atomic beam into the Zeeman tube with the aid of 20 cm of transverse collimation and cooling.

1. The atomic collimator

To optimize coupling of atoms from the source into the Zeeman-slower region, we employ an atomic collimator, with a large transverse capture velocity, which acts to uniformly decelerate the transverse velocity of the atoms over its entire length.[14,15] As shown schematically in Fig. 1(b), and in a detailed view in Fig. 3, the first 15 cm of transverse

collimation is accomplished by two pairs of nearly plane-parallel 15×2.5 cm mirrors (one pair for each transverse axis), with a 2×1 cm laser beam for each axis coupled into one end of the structure at a small angle (β_0) relative to the mirror's normal [as shown for a single pair of mirrors in Fig. 1(b)]. By using multiple reflections down the length of this cavity, we may effectively apply a radiation pressure force throughout this entire region without the need for excessively large optics or unreasonably large power requirements. With correct choice of beam and mirror geometry, we may greatly increase the capture velocity of the collimator relative to 2D molasses of comparable length.

In each pair, the two mirrors are set to deviate from a perfectly plane-parallel geometry by a small relative angle α (see Fig. 3). Thus, upon the nth reflection, the laser beam angle with mirror normal (β_n) is

$$\beta_n = \beta_0 - n\alpha. \tag{1}$$

By design, as the atomic beam propagates through the collimator, it becomes more and more collimated due to the radiation pressure from the laser beams, which become more and more normal to the mirrors according to Eq. (1).[14] In this way, it is possible for the laser beams to remain orthogonal to the trajectory of the atoms, which are then uniformly accelerated radially with the maximum spontaneous radiation pressure force $F_{\text{spont}}^{\text{max}}$, and follow an approximately circular arc characterized by a radius of curvature

$$r(v) = \frac{mv^2}{fF_{\text{spont}}^{\text{max}}}. \tag{2}$$

Here, f is the average oscillator strength of the atomic transition used. This results in a maximum capture angle for a given collimator length Δz_{cool} given by

$$\sin\theta_{\text{max}} = \frac{fF_{\text{spont}}^{\text{max}}}{mv^2}\Delta z_{\text{cool}}. \tag{3}$$

As one would expect, larger longitudinal velocity atoms have a larger radius of curvature for a given applied force, and a smaller critical angle θ_{max} (relative to the atomic beam axis).

2. Theoretical flux enhancement from collimation

In our system, the length of the transverse collimation section is 15 cm and f is 0.46 for a linearly polarized light field resonant with the $F=2$ to $F'=3$ transition of ^{87}Rb (averaged over all $\Delta m=0$ transitions). Using the 0.1 radian emission half-angle of the candlestick source for θ_{max} yields $v_{\text{crit}}=270$ m/s. Thus, for atoms with longitudinal velocities less than this value, we expect a 100% efficiency for coupling into the Zeeman slower. The flux enhancement factor from this ideal collimation procedure is the ratio between the solid angle subtended by the source emission (with half-angle of 1/10 radian) and that subtended by the Zeeman slower (a 4 cm aperture which lies 1.5 m from the emission hole, corresponding to a half angle of 1/75 radian). This results in an anticipated enhancement factor of $\eta_0=56$ for $v < v_{\text{crit}}$.

For $v > v_{\text{crit}}$, we compute $\theta_{\text{max}}(v)$ using Eq. (3) to find what fraction of the atomic beam will be collimated. In this regime, the collimated fraction is proportional to the cap-

tured solid angle $\Omega(v) \propto \theta_{max}(v)^2$. Thus, using Eq. (3), we note that the falloff in efficiency should scale as $1/v^4$. The velocity-dependent flux enhancement is

$$\eta(v) = \begin{cases} \eta_0, & v < v_{crit}, \\ \eta_0 \left(\dfrac{v_{crit}}{v} \right)^4, & v \geqslant v_{crit}. \end{cases} \quad (4)$$

In addition to computing the enhancement factor from collimation, we may ask how the expected transverse distribution of the atomic beam is modified. Assuming that the atoms are deflected by the collimation lasers onto a circular arc with radius given by Eq. (2), an atom emitted at the source with angle θ_{max} will travel 8 mm transversely by the time it exits the collimator. When we take into account that the collimator lies nearly 3 cm from the source, we anticipate that the transvere profile of the atomic beam exiting the collimator has a full width of 2 cm.

3. Expected deviation from optimum

One can readily show that with flat mirrors it is impossible to make the collimating laser wave fronts follow the perfectly circular arc shown in Fig. 3(a). In this idealized situation, we would have $\beta(z)$ vary according to

$$\beta(z) \approx \left(1 - \frac{z}{\Delta z_{cool}} \right) \beta_0 \quad (5)$$

in the limit of small β_0. In contrast, in the situation shown in Fig. 3(b),

$$\beta(z) \approx \beta_0 \sqrt{1 - \frac{z}{\Delta z_{cool}}}. \quad (6)$$

Thus we see that for uniform circular motion, β should decrease linearly with increasing z, but that using multiple reflections on flat mirrors will only locally approximate this behavior and lead instead to a decrease as $\sqrt{\Delta z_{cool} - z}$. This corresponds to a constantly changing radius of curvature of the optical wave front formed by the combined multiply reflected laser beams,

$$r_{FM}(z) \approx r_c \sqrt{1 - \frac{z}{\Delta z_{cool}}}, \quad (7)$$

which decreases with increasing z, causing the wave front to form an increasingly tighter arc. If $r_{FM}(z) < r(v)$ from Eq. (2), a force greater than F_{max}^{spont} would be required to deflect the atoms onto this trajectory. Thus, for fixed force and fixed distance Δz_{cool}, this drop in radius will manifest itself as a decrease in v_{crit} for optimal collimation.

Although the laser rays will not follow the ideal trajectory as a function of z, the increasingly steep angle at which they reflect will cause the density of the rays to increase at the end of the collimator, compensating for the laser intensity loss from repeated reflections and background-atom absorption. Without this effect, the laser power at the end of the collimator would be significantly attenuated, and we would suffer a decrease in efficiency as $F < F_{spont}^{max}$.

As a final consideration, we require the laser beam to exit the collimator; if the laser beam at the end of the collimator is normal to the mirror, the beam will simply couple
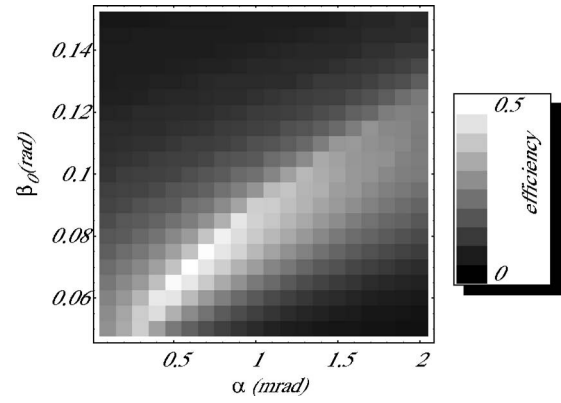

FIG. 4. Plot of theoretical collimation efficiency vs β_0 and α. Computed by assuming the actual form of the propagation angle [Eq. (6)] and using classical forces for all of the reflected laser beams. The efficiency is the fraction of atoms emitted by the source with velocity less than 320 m/s that are sufficiently collimated to make it through the Zeeman slower.

back down the cavity and undo the collimation. To avoid this, we apply the laser beam slightly nonorthogonally to the atomic velocity and correct for the resulting longitudinal Doppler shift by blue detuning the laser by +3 MHz ($0.5\Gamma/2\pi$, where Γ is the natural linewidth).

This solution induces a side effect, however, as the Doppler shift of the atoms relative to the collimating laser beams will depend on their longitudinal velocity (since the +3 MHz is chosen to optimally address the most prevalent atoms at around 200–300 m/s). The slower atoms will experience a positive laser detuning at the end of collimator and will consequently be defocused. Numerical simulations have shown that this happens for longitudinal velocities smaller than 50 m/s, corresponding to only a small fraction of the emitted atoms. As a result, we anticipate that the detuning will lead to just a small net decrease in the overall efficiency of collimation for smaller velocities.

To account for these loss mechanisms, we have undertaken a detailed theoretical study of the efficiency of the collimation structure. The simulation treats the forces due to the laser fields as classical in nature (neglecting effects from spontaneous emission) and uses the form of $\beta(z)$ given above in Eq. (6) to define the propagation direction. Attenuation effects (from mirror losses and atomic absorption) due to multiple reflections are included. A plot of the total efficiency of collimation as a function of the initial coupling angle β_0 and the relative mirror tilt α is shown in Fig. 4. Here, we define the efficiency parameter to be the fraction of atoms emitted by the source with velocities within the 320 m/s capture range of the Zeeman slower that are sufficiently collimated to pass through the Zeeman-slower aperture. The theoretical efficiency is as high as 50% with the proper choice of parameters. This optimum occurs at the coupling angle $\beta_0 \approx 0.1$ rad and a relative mirror tilt of only 1 mrad, with a factor of 2 drop in efficiency within $\Delta\alpha = 250$ μrad on either side of this optimum. For maximum efficiency, controlling this relative angle to within these tolerances is imperative. We discuss the implementation of this design in Sec. II B 5.
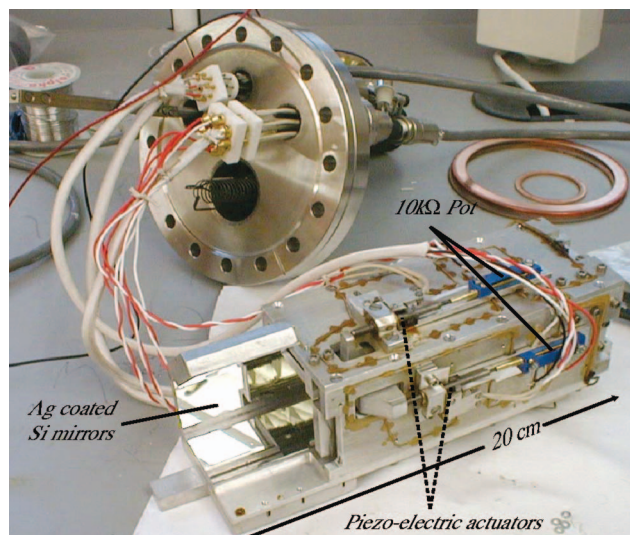
FIG. 5. Transverse collimator and mounting flange. Laser beams for collimation described in Sec. II B 1 are coupled in at the extreme right and traverse the collimation region with 50–100 reflections. Relative tilt of the mirrors is adjusted by four piezoelectric actuators, with the top and side longitudinal ones shown. These actuators define α in Eq. (1). Additional 5 cm long mirrors at the left of the collimator are used for the 2D molasses, which are used in single back-reflection.

4. Optical molasses

The orientation of the entire transverse collimation and cooling structure must be optimized to couple the atomic beam into the Zeeman slower. The Zeeman-slower tube creates an aperture with a solid angle of only 10^{-3} sr with respect to the candlestick's emission hole, which sets the tolerance for this orientation.

The whole optical collimation structure is kept in vacuum and can be tilted vertically and horizontally with a pair of linear feed-throughs. With the tight tolerances on β_0 and α for maximum efficiency discussed in the previous section, this ability to decouple the pointing of the whole structure from the fine tuning of these two angles is essential for practical alignment. Thus, as a final step, the transverse collimation stage is followed by approximately 5 cm of 2D optical molasses, tuned 5 MHz below resonance [Fig. 1(c)]. Experimentally, this 2D molasses produces a sufficient flux enhancement in the detection chamber to allow for the alignment of the whole structure before the final alignment of the atomic collimator's beams and mirrors (β_0 and α).

In addition to aiding in overall alignment, this section of molasses has beneficial effects on the atom beam's transverse temperature; although we are able to greatly increase the flux with the atomic collimator, the laser beams in this region are chosen to be close to resonance. As a result, as the laser beams exit the collimator at a near-normal angle, they set up a near-resonant molasses, leading to a final transverse temperature much larger than the Doppler limit. Addition of a 2D molasses compensates for this and further increases the overall beam flux.

5. Design of the collimation structure

A picture of the actual collimation structure is shown in Fig. 5. *In situ*, the structure is mounted on two linear translation vacuum feed-throughs, each of which is responsible for the tilting of the structure along one axis. During the feed-through alignment, only the 2D molasses region (at left in the figure) is activated while the structure is tilted to optimize the flux signal in the detection chamber.

The mirrors are cut from a silicon wafer, which has the advantage of being optically flat over large distances as well as being comparatively inexpensive and thin. The reflecting surface is formed by thermally evaporating 220 nm of silver on top of 17 nm of chromium, which serves as an adhesion layer. The mirrors are then overcoated with 40 nm of MgF_2 to protect the silver from oxidization prior to assembly and chamber pump-down. We produce mirrors with reflection coefficients better than 99% at 780 nm. (Note that gold has a slightly better reflection coefficient at this wavelength, but it has the disadvantage of readily forming alloys with all the alkalis.)

To tilt the mirrors in vacuum with the high precision required for optimization of the angles β_0 and α, we have equipped one mirror in each pair with two piezoelectric actuators.[19] Each actuator comes encased in an anodized aluminum sheath, which can be removed along with its connector block to make them UHV compatible. The electrical connector is bypassed and the actuator's electrodes were soldered directly to Teflon®-insulated wire.[20] Finally, the actuators are disassembled and the thread lubricant was cleaned off and replaced with vacuum grease.[21]

One actuator in each pair is used to align the cavity transversely, while the second sets the longitudinal tilt α defined in the previous section. Each actuator consists of an 80 TPI screw that may be turned with milliradian accuracy, leading to a positioning precision of tens of microradians for each mirror's longitudinal tilt. To allow for positioning repeatability and readout *in situ*, each longitudinal actuator shaft is tied to the screw of a 10 kΩ ten-turn potentiometer.[22] By applying 5 V across each pot, we generate a signal of about 100 mV/mrad of mirror tilt.

As a final consideration, the structures in the source chamber must remain as clean as possible. Deposition of Rb on the mirrors or the actuators is detrimental from an optical and electrical standpoint, respectively. To avoid this problem, a heater strip consisting of a single piece of stainless steel wire is thermally epoxied[23] to the outside of the collimation structure. While in operation, the structure is maintained at a temperature between 40 and 50 °C to ensure evaporation of any Rb deposits. This heating, in addition to the cryopumping described in the following section, maintains the required cleanliness of the source chamber.

The whole structure can be baked as high as 100 °C for several days during a bake cycle. To avoid stress from differences in thermal expansion between the silicon mirrors and the aluminum frame of the collimator, the mirrors were mounted using molybdenum wire spring-clamps that press the mirrors onto their mounts, but allow them to slide freely. Prior to Rb loading, chamber base pressures as low as 8 $\times 10^{-10}$ Torr have been achieved with the whole structure assembled and in place, and pumped solely with a 150 L/s turbo pump.

6. Cryopumping with a cold finger

The pressure of the source vacuum chamber can be kept below 10^{-8} Torr, with the aid of a -45 °C cold finger, which is implemented with a stacked TEC and water-cooled baseplate. The cold side of the TEC is in contact with a 0.5 in. solid copper feed-through, which attaches to a shroud that extends around the back of the candlestick source, covering nearly 2π of solid angle, with a total surface area of more than 200 cm^2. When it is cooled, the pressure in the source chamber drops by a full order of magnitude.

In addition to being beneficial for the overall cleanliness of the vacuum chamber, the low pressures achieved with the help of the cold finger are critical for the operation of the transverse collimator. At a rubidium partial pressure of 10^{-7} Torr, the $1/e$ attenuation length of a nonsaturated on-resonant laser beam is approximately 10 cm, corresponding to only 2.5 reflections inside the transverse collimator. Even for the intense cooling laser beams we employ, there would be significant attenuation of the light fields even over a small fraction of their way down the collimator. Reducing the pressure of the chamber to 10^{-8} Torr increases the attenuation length to 1 m (or about 25 reflections) and, in fact, ensures that the primary absorption is caused by the atomic beam itself and not the background vapor.

C. The addition of the Zeeman slower

With the atomic beam collimated, transversely cooled, and efficiently coupled out of the source chamber, the actual beam slowing and longitudinal cooling are accomplished with a 1 m long Zeeman slower that is designed to have a maximum capture velocity of 320 m/s [Fig. 1(d)]. The Zeeman slower incorporates a spatially varying magnetic field that Zeeman shifts the atoms' resonance to compensate for the decreasing Doppler shift of a counterpropagating laser beam (in the rest frame of the atoms).[8] The field of the slower and the coil design are given in Fig. 1(b). We choose a zero-crossing design to minimize field leakage into the detection chamber and to keep electrical power requirements as low as possible (at 6 A, the coils dissipate less than 60 W).

By design, the last six coils (which produce the "negative" part of the field profile) can be driven independently of the top thirteen. Since the final velocity of the atoms is set by the final value of the magnetic field in the slower (via the resonance condition $k_0 v_{\text{final}} = -\Delta_Z + \mu_B B_{\text{final}}/\hbar$, with $\Delta_Z < 0$ the detuning of the Zeeman-slower laser and k_0 the photon wave number), this scheme allows us to continuously change the final velocity of the atomic beam without affecting the capture velocity of the slower. Finally an atom to be decelerated from 300 to 40 m/s, the atom must scatter approximately $m(v_0 - v_f)/\hbar k_0 \approx 40\,000$ photons. Thus, for a total flux of 10^{13}/s, a total power of approximately 100 mW is required to decelerate the atoms.

D. Optics setup

In the present setup, our primary source of laser power is a 2 W Ti:Sa laser (Coherent MBR-110) which is frequency locked near the $F=2$ to $F'=3$ transition of the ^{87}Rb D_2 mani-

fold. We use 150 mW at $\Delta/2\pi = +3$ MHz for the atomic collimator's two beams (with a 5 mm waist in the longitudinal direction and a 12 mm waist transverse to the beam), and 100 mW at $\Delta/2\pi = -5$ MHz for the molasses (with a 24 mm longitudinal and 12 mm transverse waist). The Zeeman-slower beam is detuned 180 MHz below resonance and uses 60 mW of power with a 25 mm waist. Finally, for our probe laser beam, we use a 2 μW beam with a diameter of 1.5 mm (saturation parameter of 0.1) which can be continuously tuned over a range from -200 to $+40$ MHz to sample the velocity distribution of the atomic beam.

To generate laser light to repump atoms that end up in the $F=1$ ground state, we use a pair of diode lasers that are locked to the $F=1$ to $F'=2$ transition on the D_1 manifold. One diode (the "master," a 30 mW Sharp LT024MD0) is stabilized via an external grating to the atomic resonance. Power from this laser is used to injection lock a "slave" laser.[24] The resulting repumper power is split into 7 mW for a Zeeman repumper (detuned by -180 MHz from resonance like the Zeeman beam itself) and 7 mW for a transverse cooling repumper (with 1 mW for molasses and 6 mW for the atomic collimator). This leaves 10 mW for repumping in the detection region, where we send the repumper beam in normal to the atomic beam (into the page according to Fig. 1) and tuned to resonance so that it is velocity insensitive, pumping all atoms in the detector region equally.

III. DETECTION VIA ABSORPTION

We first directly demonstrate the effectiveness of the atomic-beam collimation stage by performing an absorption measurement in the detection chamber without the magnetic field or Zeeman-slowing beam present. By measuring the transmission coefficient of a probe laser through the atomic beam, we may extract the optical density (OD) of the atomic beam. Further, by sweeping the detuning (Δ) of the probe laser, we extract the atomic-beam's velocity distribution projected onto the probe's axis [see Fig. 1(e)].

A. Flux enhancement through transverse cooling

Data resulting from the above method are shown in Fig. 6(a). In this case, the probe is normal ($\phi=0°$) to the axis of the atomic beam, so that we may discern the transverse velocity spread. We find that the addition of transverse collimation and cooling indeed decreases the velocity spread and significantly boosts the overall signal.

By fitting the frequency profile of the optical density OD to a Voigt distribution, as

$$\text{OD}(\Delta) \propto \int n(v_x) \sigma(\Delta - k_0 v_x) dv_x, \tag{8}$$

we may extract the velocity spread of the distribution $n(v_x)$, given the Lorentzian form of the absorption cross section $\sigma(\Delta)$ (where v_x is the transverse velocity and k_0 the wave number). The uncollimated emission from our source has velocity spread of 4 m/s in the detection chamber, which is simply a consequence of geometry (an atomic beam with a mean longitudinal velocity of around 400 m/s apertured to a half-angle of 1/100th of a radian by the Zeeman slower
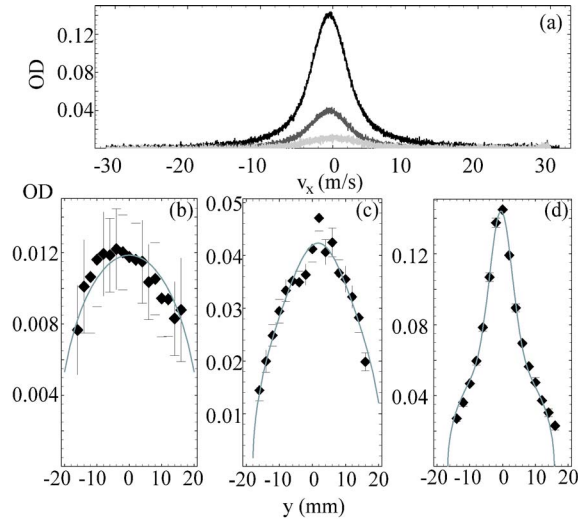
FIG. 6. Measurement of the atomic beam's transverse velocity and spatial distributions. (a) OD of the bare atomic beam (light gray), with molasses (dark gray), and with the full 20 cm of transverse collimation and cooling (black). (b)–(d) Transverse structure of the atomic beam obtained by scanning the position of the probe beam along the direction normal to the Zeeman slower axis and the probe beam direction. This is done for the (b) uncollimated atomic beam, (c) with 2D molasses, and (d) with the full 20 cm of transverse cooling and collimation.

tube). Addition of the 2D molasses decreases this spread to 1.7 m/s, while the application of the full transverse collimation and cooling leads to a velocity spread of only 1 m/s. However, this spread is so small that it is approaching the sensitivity of our measurement, determined by the natural linewidth of the probe transition. In this low-transverse-temperature regime, a better measurement of the transverse velocity spread gives 0.5 m/s (described in Sec. III C and Fig. 9 below).

As an extension of this method, in Figs. 6(b)–6(d), we translate the probe laser along y and measure the peak OD at each y-position to extract the transverse structure of the atomic beam. Consider first the simple case that the atomic beam is uniformly distributed in the transverse (x,y) plane. In this case the profile of the atomic beam would be a disk defined as

$$g(x,y) = N\Theta(r_0^2 - x^2 - y^2), \tag{9}$$

where $\Theta(r)$ is the unit step function, reflecting the aperturing of the Zeeman slower tube that has radius r_0, and N is the proper normalization factor. Measurement of the OD is equivalent to integrating Eq. (9) along x, so that the measurement will give the y-mode function

$$G(y) \equiv OD(y)/\int OD(y')dy' \tag{10}$$

$$\equiv \int g(x,y)dx$$

$$= 2N\sqrt{r_0^2 - y^2}\,\Theta(r_0^2 - y^2). \tag{11}$$

In Fig. 6(b) we show the measured distribution of the atomic beam with a fit to Eq. (11).

As a simple extension of the result for a uniform distribution, we consider what happens to the y profile of the

atomic beam with the addition of transverse collimation and cooling. We may presume that the transverse profile should take the form

$$g(x,y) = (N_1 + N_2 e^{-(x^2+y^2)/2\sigma^2})\Theta(r_0^2 - x^2 - y^2), \tag{12}$$

where the Gaussian (on top of a uniform background given by N_1) is a consequence of the atomic-beam collimation and cooling, and Θ still indicates the aperturing of the distribution due to the Zeeman-slower tube. In this case, projection along x will lead to a distribution of the form

$$G(y) = \left[2N_1\sqrt{r_0^2 - y^2} + N_2 e^{-y^2/2\sigma^2}\sigma^2\mathrm{Erf}\left(\sqrt{\frac{r_0^2 - y^2}{2\sigma^2}}\right)\right]$$
$$\times \Theta(r_0^2 - y^2). \tag{13}$$

Figures 6(c) and 6(d) show the data and corresponding fits using Eq. (13) with 2D molasses and with full transverse collimation and cooling, respectively. In all three situations [Figs. 6(b)–6(d)], the radius r_0 of the disk is left as a fit parameter, and yields a value near the actual 1.9 cm radius of the Zeeman vacuum tube.

The peaked structure in Fig. 6(d) is consistent with the theory presented in Sec. II B 2. We anticipated that atoms within the $1/10$th radian divergence of the source and with velocity less than the critical velocity would be swept into a disk of diameter approximately 2 cm (or about half the size of the Zeeman aperture). Here, the fit yields a Gaussian 2σ full width of 1.2 cm, consistent with our earlier prediction.

B. The longitudinal velocity distribution

To measure the longitudinal velocity spread, we switch to a detection geometry in which the probe is at an angle $\phi=9°$ relative to the normal of the atomic beam. With the detection axis tipped away from normal, and the ability to vary the probe laser detuning, it is possible to measure the optical density as a function of longitudinal velocity rather than transverse (Fig. 7 inset). The bottom (light gray) curve represents the signal from the uncollimated distribution from the source. The middle (dark gray) and top (black) curves represent the addition of the 2D molasses and full transverse cooling and collimation, respectively. As anticipated, both of these transverse cooling configurations work best at lower longitudinal velocities, but still give significant enhancement up to 300 m/s.

To extract the flux density, $\Phi_{meas}(v_z)$ [which has units of $(number/s)/(m/s)$] from this measurement, we must note first that the measurement is sensitive to the column density, defined as

$$N_{coil}(v_z,y) \equiv \frac{\Phi_{meas}(v_z)}{v_z}\frac{1}{\cos\phi}G(y). \tag{14}$$

Here, v_z is the longitudinal (z) velocity component. The corresponding expression for the Voigt distribution may be written as

$$OD(\Delta,y) = f\sigma_0\int dv_z\frac{N_{col}(v_z,y)}{1 + (4/\Gamma^2)(\Delta - k_0 v_z \sin\phi)^2}. \tag{15}$$

We have assumed that the intensity of the probe is much less than the saturation intensity of the atomic transition used, Δ
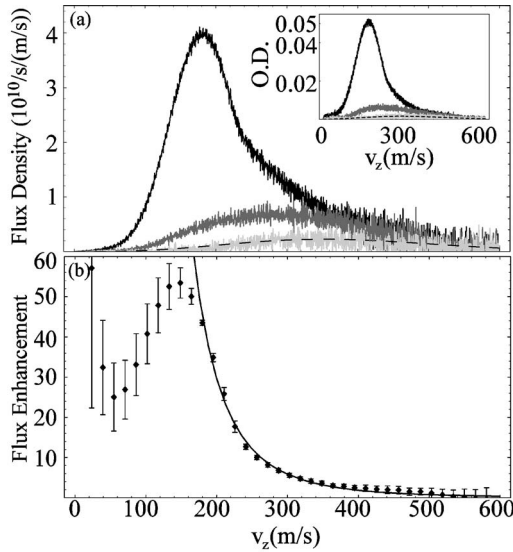
FIG. 7. Flux enhancement through transverse collimation and cooling. (a) Flux measured as a function of longitudinal velocity based on measurement of the OD as a function of probe frequency (inset). The color scheme here is as in Fig. 6(a). The dashed curve is a calculation of the distribution solely from effusion from the source at $T=160\ ^{\circ}$C (no adjustable parameters). (b) the flux enhancement as a function of velocity produced by the transverse collimation and cooling scheme. Here, the points are a result of dividing the optimally collimated (black) curve in (a) by the expected effusion (dashed) to get the flux enhancement. The solid curve represents a fit to a $1/v^4$ falloff for the tail.

is the detuning of the probe from resonance, Γ the natural linewidth, and σ_0 the resonant cross section of a two-level transition, which is weighted by the average oscillator strength f. (For our purposes, the probe is linearly polarized, with a peak intensity $I \lesssim 0.1\ I_{\text{sat}}$, while $f \approx 0.46$, found by averaging over the available $5S_{1/2}\ F=2$ to $5P_{3/2}\ F=3$ transitions.)

In practice, deconvolving the measured OD distribution to extract the flux density is nontrivial. However, in the limiting case where the width of the measured OD (Δ) distribution is much larger than Γ, we accordingly assume that the spread in $N_{\text{coll}}(v_z)$ is much larger than $\Gamma/k_0 \sin\phi \approx 36$ m/s (as one would expect from a thermal distribution). We thus ignore the variation of $N_{\text{coll}}(v_z)$ for the purposes of integration and correspondingly pull it outside the v_z integral. Integrating what is left and rearranging leads to an expression for Φ_{meas} in terms of the measured OD,

$$\Phi_{\text{meas}}(v_z) = \frac{2k_0 v_z \sin\phi \cos\phi}{f\sigma_0 \Gamma \pi} \frac{\text{OD}(k_0 v_z \sin\phi, y)}{G(y)}. \quad (16)$$

Thus, we readily obtain the atomic beam's flux density from the OD measurement. The result is shown in Fig. 7(a). In this figure, the dashed curve represents the expected signal from atoms that make it to the detection chamber in the absence of transverse collimation and cooling, and is given according to an effusive distribution[25]

$$\Phi_{\text{effus}}(v_z) = A \frac{P_{\text{vap}}(T)}{k_B T} \frac{m^3 v_z^3 e^{-mv_z^2/2k_B T}}{(2\pi m k_B T)^{3/2}} \int_{\Delta\Omega} d\Omega \cos\theta. \quad (17)$$

Here, $\Delta\Omega$ is the solid angle subtended by the Zeeman slower from the emission hole, T is the temperature at the emission

point, $P_{\text{vap}}(T)$ the corresponding vapor pressure of ^{87}Rb, and A the surface area of the emission hole. [Note that there are no free parameters in determining the dashed curve $\Phi_{\text{effus}}(v_z)$, and that it agrees completely with our data. We have observed deviations from Eq. (17) for emission temperatures above 170 $^{\circ}$C, where the atom beam becomes supersonic.]

From this, we extract the flux enhancement factor [Eq. (4)] from transverse collimation and cooling as a function of longitudinal velocity, as shown in Fig. 7(b). Here, we divide the measured flux density of the fully collimated and transversely cooled distribution Φ_{meas}, by the expected distribution Φ_{effus} in Eq. (17). The optimum of this distribution completely agrees with the theoretical enhancement factor of $\eta_0 = 56$ and the falloff is fit well by $1/v^4$.

Moreover, as predicted in Sec. II B 3, though the overall efficiency drops off for lower velocity atoms (because of the blue detuning of the atomic collimator laser beams) the capture efficiency as a function of velocity is 50% or better for a broad range of longitudinal velocities spanning 150 m/s. The fit to $1/v^4$ allows us to extract the actual $v_{\text{crit}} \approx 170$ m/s of the system, which shows that the average collimating radiation pressure force is approximately a factor of 2 smaller than optimal.

The overall efficiency of the transverse collimation and cooling process can be summarized as follows: of the 1.1×10^{13}/s that are "capturable" by the Zeeman slower (those emitted with a velocity of less than 320 m/s), only about 2×10^{11}/s would arrive in the detection chamber as a result of the solid angle subtended by the Zeeman aperture alone. Transverse collimation and cooling increases this capturable flux to 5.3×10^{12} atoms/s obtained by calculating the area under the measured (black) distribution in Fig. 7(a). This factor of 25 enhancement implies that a full 50% of the atoms that are usable from our source can be coupled through the Zeeman-slower structure.

C. The effect of the Zeeman slower

With the atomic beam transversely cooled and collimated, the Zeeman slower is employed to longitudinally decelerate and cool the atomic beam, as described in Sec. II C. The measured effect of the Zeeman slower on the atomic beam with various magnetic field configurations is shown in Fig. 8. Recall that the coils at the top of the slower determine the maximum capture velocity, while the independently controlled coils at the bottom adjust the final output velocity. In this series, we choose our probe beam to be at 45° to the axis of the atomic beam, to allow for maximum velocity sensitivity.

Unlike the situation in the previous section, the width of the measured distribution with the activation of the Zeeman slower is small relative to the atomic linewidth. In this case, we may approximate the expression for the measured optical density in Eq. (15) as
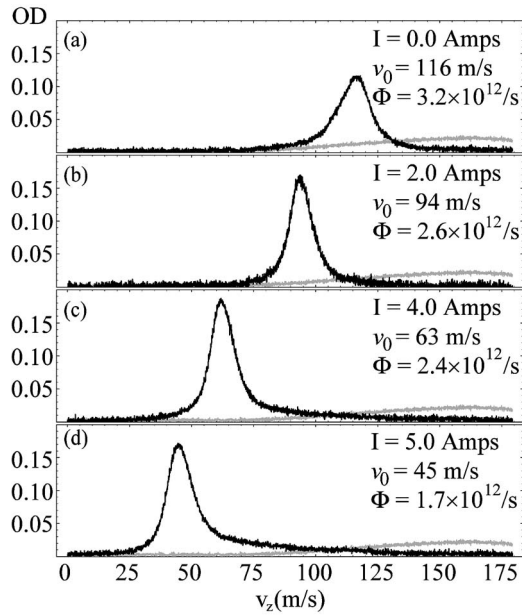
FIG. 8. Optical density measurement of Zeeman slowed atomic beam, taken at a probe angle of 45° relative to the atomic beam axis for varying final velocities. In all cases, the current in the top 13 coils of the slower is maintained at 5 A (corresponding to a capture velocity of 320 m/s). The current I in each plot is that of the final set of Zeeman-slower coils, which adjust the final velocity by 16 (m/s)/A. The gray curve represents the same situation as the black curve in Fig. 7.

$$\text{OD}(\Delta, y) \approx \frac{f \sigma_0 G(y)}{v_0 \cos \phi} \int dv_z \frac{\Phi_{\text{meas}}(v_z)}{1 + (4/\Gamma^2)(\Delta - k_0 v_z \sin \phi)^2}; \tag{18}$$

that is, we take advantage of the fact that the velocity distribution is sharply peaked around a particular velocity v_0, to substitute $1/v_0$ for $1/v_z$. Equation (18) is a convolution integral and, since convolutions are norm preserving, we get an expression for the total flux:

$$\int \Phi_{\text{meas}}(v_z) dv_z = \frac{2 v_0 \cos \phi}{f \sigma_0 \Gamma \pi G(y)} \int \text{OD}(\Delta, y) d\Delta. \tag{19}$$

Thus, by measuring the spatial distribution of the atomic beam in each case (as shown in Fig. 9) in the same manner as described in Sec. III A, we may readily compute the total flux of the atomic beam.

In Fig. 8(a) we show the effect of turning on the positive field region of the Zeeman slower [as defined by the first 13
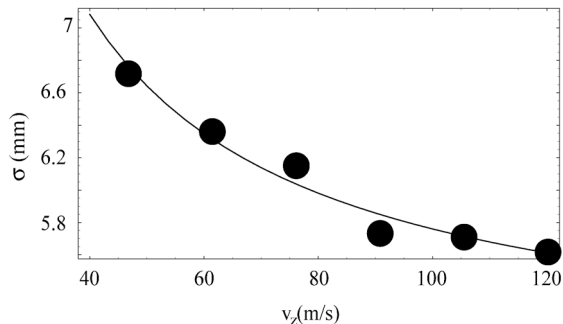

FIG. 9. Decelerated atomic beam radius versus final velocity. The points are fit to a linear function of $1/v$ to extract the transverse velocity.

coils in Fig. 1(d)]. The Zeeman-slower laser beam is negatively detuned by 180 MHz and thus resonantly couples to atoms that are traveling at 150 m/s in zero magnetic field. The peak in Fig. 8(a), however, is at 115 m/s, which clearly shows that without activation of the lower half of the Zeeman slower, the atomic beam continues to scatter photons from the slowing beam and to decelerate all the way into the detection region.

As the field is further increased, as shown in Figs. 8(b)–8(d), we are able to continuously tune the final velocity of the atomic beam, while always maintaining a high overall flux. In these figures, the stated flux in each case corresponds to the total flux underneath the main peak fit by a Voigt distribution (not shown). From this fit we also obtain a longitudinal velocity spread of 3 m/s, comparable to a longitudinal temperature of 90 mK.

As we proceed to lower final velocities, the flux in the main peak drops slightly and the distribution begins to form a high-velocity tail. In fact, integrating the total distribution (up to 150 m/s) yields a total flux of 3×10^{12} atoms per second in all four cases; the presence of the high tail has been traced to "bumps" in the magnetic field at the end of the Zeeman slower (corresponding to transitions between individual coils).

Our measurements of the transverse size of the atomic beam as a function of final longitudinal velocity can be used to derive a more direct estimate of the transverse velocity spread than that found by fitting to a Voigt distribution as in Sec. III A. As shown in Fig. 9, by fitting the beam's radius to a falloff linear in $1/v$, we obtain a transverse velocity spread of 0.5 m/s, corresponding to a transverse temperature of 3 mK. With a Doppler cooling limit of 0.12 m/s for rubidium, the predicted spread is dominated by transverse heating from spontaneous emission events during Zeeman slowing. The latter gives a spread of $\sqrt{(v_0 - v_f) v_{\text{recoil}}} \approx 1$ m/s, in good agreement with the measured value.

Moreover, the signal enhancement to the Zeeman-slowed distribution by means of transverse cooling and collimation actually exceeds the factor of 25 observed from the transverse cooling prior to Zeeman slowing. Without the addition of the transverse collimator, the atomic beam will spread rapidly as it is decelerated by the Zeeman slower, and we will lose flux as the atoms hit the Zeeman vacuum tube. Addition of transverse cooling prior to Zeeman slowing, however, freezes out almost all of the transverse momentum of the atomic beam, so that we see $3.2 \times 10^{12} (1.7 \times 10^{12})$ atoms/s at 115(45) m/s, to be compared to $6 \times 10^{10} (3 \times 10^{10})$ atoms/s in the absence of transverse cooling, for a factor of 50 increase in overall flux. The flux and density characteristics of the resulting atomic beam are summarized in Table I.

IV. CONCLUSION

A design consisting of a matched combination of a candlestick atomic beam source with a 20 cm long atom collimator and a 1 m long Zeeman slower has lead to the production of a continuous, cold atomic beam with a high flux. We believe this high-flux source will be of decisive impor-

TABLE I. Beam characterization parameters, based on experimentally determined values for flux Φ, longitudinal peak velocity v_z, spread Δv_z, $g(0,0)$ the normalized peak beam intensity as defined from Eq. (12), and Ω the solid angle given by the beam's divergence.

Quantity	Definition	$v=115$ m/s	$v=45$ m/s
Flux (s^{-1})	Φ	3.2×10^{12}	1.7×10^{12}
Intensity $(s\ cm^2)^{-1}$	$I=\Phi g(0,0)$	7.9×10^{11}	3.1×10^{11}
Density (cm^{-3})	$n=I/v_z$	6.8×10^{7}	7.1×10^{7}
Brightness $(s\ cm^2\ sr)^{-1}$	$R=I/\Omega$	3.3×10^{15}	2.1×10^{14}
Brilliance $(s\ cm^2\ sr)^{-1}$	$B=Rv_z/\Delta v_z$	4.5×10^{16}	1.1×10^{15}

tance in the quest for the production of a cw atom laser: a continuous source of coherent and cold atoms, which is considered a "holy grail" in atomic physics. It would be of great importance for atom optics experiments, for example as a source for atom-interferometer based gyroscopes.

ACKNOWLEDGMENTS

[1] P. R. Berman, *Atom Interferometry*, 1st ed. (Academic, London, 1997).
[2] Z. T. Lu *et al.*, Phys. Rev. Lett. **77**, 3331 (1996).
[3] K. I. Lee *et al.*, J. Korean Phys. Soc. **33**, 365 (1998).
[4] E. Riis, D. S. Weiss, K. A. Moler, and S. Chu, Phys. Rev. Lett. **64**, 1658 (1990).
[5] K. Dieckmann, R. J. C. Spreeuw, M. Weidemüller, and J. T. M. Walraven, Phys. Rev. A **58**, 3891 (1998).
[6] W. Wohlleben, F. Chevy, K. Madison, and J. Dalibard, Eur. Phys. J. D **15**, 237 (2001).
[7] S. E. Park *et al.*, J. Opt. Soc. Am. B **19**, 2595 (2002).
[8] J. V. Prodan, W. D. Phillips, and H. Metcalf, Phys. Rev. Lett. **49**, 1149 (1982).
[9] P. D. Lett *et al.*, J. Opt. Soc. Am. B **6**, 2084 (1989).
[10] F. Lison, P. Schuh, D. Haubrich, and D. Meschede, Phys. Rev. A **61**, 013405 (1999).
[11] T. Lahay *et al.*, Phys. Rev. Lett. **93**, 093003 (2004).
[12] L. V. Hau, J. A. Golovchenko, and M. M. Burns, Rev. Sci. Instrum. **65**, 3746 (1994).
[13] M. R. Walkiewicz, P. J. Fox, and R. E. Scholten, Rev. Sci. Instrum. **71**, 3342 (2000).
[14] A. Aspect *et al.*, Chem. Phys. **145**, 307 (1990).
[15] M. D. Hoogerland *et al.*, Appl. Phys. B: Lasers Opt. **62**, 232 (1996).
[16] 250×250 OPI, 0.0016 in. wire, Type 316 stainless steel mesh from Unique Wire Weaving, Inc., Hillside, NJ.
[17] Orosene 999 Gold Solution, from Technic, Inc., 0.125 tr oz Au/$(\frac{1}{2}L)$, Cranston, RI.
[18] From Alfa Aesar, part # 10073. Unlike pure tungsten wire, the W:Re does not suffer from problems with brittleness after repeated thermal cycling, Ward Hill, MA.
[19] Picomotor actuator, 8351 from Newfocus, Inc., San Jose, CA.
[20] Stranded 22 AWG Teflon®-insulated wire, Part # 2122/19 from Weico Wire and Cable, Edgewood, NY.
[21] Dupont Krytox®, Wilmington, DE.
[22] Ten-turn 10 K pot, 3059Y-103-ND from Digikey. To make it vacuum compatible, pots were slotted on the screw side to prevent closed volumes or virtual leaks, Thied River Falls, MN.
[23] H77 thermally conductive UHV compatible epoxy from Epoxy Technology, Inc., Billerica, MA.
[24] 50 mW, from Semiconductor Laser International, Co., SLI-CW-9MM-C1-795-0.08S-R, Binghamton, NY.
[25] C. Kittel and H. Kroemer, *Thermal Physics*, 2nd ed. (W. H. Freeman, New York, 1980).